Low coherence interferometry using microwave photonics for multilayered samples

J. Benítez and J. Mora

Abstract—**A novel photonic structure is proposed by exploiting the advantages of the Microwave Photonics technology over conventional Low Coherence Interferometry. The proposed scheme is based in the analysis of the interference pattern of an incoherent optical signal which is amplitude modulated and transmitted through a dispersive element. The strategic allocation of an interferometric structure combined with balanced photodetection are used to improve the system performance compared to previous proposals. For the first time of our knowledge, an exhaustive theoretical analysis and an experimental demonstration of the structure for multilayered samples are provided in this work.**

Index Terms—**Fiber optics, interferometry, microwave photonics, optical inspection, optical coherence tomography.**

I. INTRODUCTION

OPTICAL Low Coherence Interferometry (LCI) constitutes an interesting measurement technique able to offer an axial positioning precision of the order of the microns [1]. In its basic configuration, the principle of operation is based on the interference produced by the combination of the light coming from the sample and a reference mirror. LCI permits to obtain valuable information about the characteristics of the sample under test through the interference fringes [2]. By analyzing the interference pattern, the measurement of the optical path difference (OPD) related to the sample may result from the variation of different physical quantities that can be thus determined. In this way, a large number of approaches have been researched and applied to different fields taking benefits of this technology, such as components characterization [3], art conservation [4] or sensing [5]. In particular, LCI has had an impressive development in the recent years due to the high interest in medical applications. One of the most exciting applications of LCI is the Optical Coherence Tomography (OCT) [6]. OCT is non-invasive, provides high depth resolution and it can be applied to different types of tissue, skin, hair, burns, etc. In this sense,

J. Benítez and J. Mora* are with the ITEAM Research Institute, Universitat Politècnica de València, Valencia, Spain (*e-mail: jmalmer@iteam.upv.es).

LCI is currently evolving quickly with applications in medical diagnosis [7-9] and ophthalmology [10, 11].

Current LCI and OCT research focuses on the improvement of key performance parameters for specific applications, in particular in terms of stability, resolution, sensitivity and scanning speed, in most cases limited to a single interferometric structure [12]. In this context, we propose the combination of Microwave Photonics (MWP) and LCI as the solution to address the limitations in LCI applications.

MWP is a promising discipline with the objective of improving the functionalities of radiofrequency (RF) engineering by means of the combination with the optical technology [13]. MWP can offer significant benefits to LCI systems due to the stability of the interference pattern in the radio-frequency (RF) domain under environmental variations without compromising overall LCI performance in relatively simple and scalable readout systems, together with a high resolution. Indeed, this observation has recently fostered the use of MWP techniques for alternative fields as sensing applications [14, 15]. Recently, MWP-LCI schemes have been proposed for retrieving the visibility of low-coherence interferograms by use of a single-passband MWP filtering structure as an alternative to double-interferometer LCI systems [16]. In this contribution, a correspondence of LCI and MWP filters has been reported in this context, thus opening the way to comparatively explore MWP structures from an LCI perspective. However, the proposed structure reduces drastically the system sensitivity in the range of frequencies affected by the Carrier Suppression Effect (CSE). Moreover, the existence of a baseband component is inherent to this system and, consequently, the penetration depth related to the axial position is doubly limited. Recently, we have proposed an alternative MWP-LCI structure by strategically allocating the interferometer structure [17]. In that case, CSE is avoided leading to a considerable penetration depth increasing and an invariant resolution in the whole measurement range is achieved compared to previous work [16]. However, the measurement range is limited for low OPDs due to the baseband component.

In this context, we aim to develop a novel MWP-LCI structure in order to overcome all limitations of previous proposals. In this manuscript, we employ an incoherent source to generate the optical signal, which is electrically modulated and introduced in an interferometric structure. Afterwards, the interference pattern produced by the OPD between the arms of the interferometer is recorded via its electrical transfer
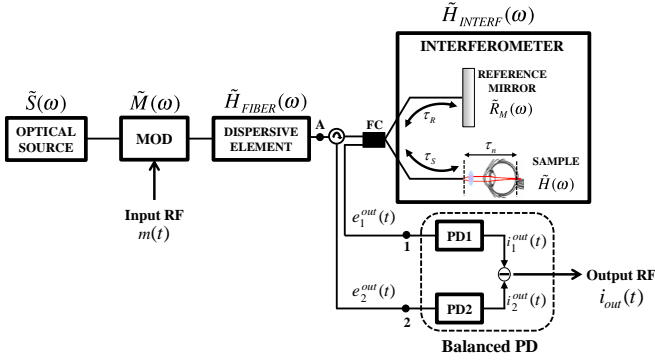
Fig. 1. General layout of the MWP-LCI scheme proposed based on a Mach-Zehnder Interferometer (MZI) with balanced detection.

function and analyzed by means of a dispersive element. A full theoretical description of the MWP-LCI proposal is presented in section 2. As far as we know, we theoretically analyze the proposed structure when a multilayered sample is considered for the first time. Previous MWP-LCI schemes are demonstrated and limited to one-layered sample. The degrading factors that are analyzed in this manuscript are not present in previous approaches. However, these previous schemes are not free from these limiting factors when multilayered samples are introduced. Then, different capabilities are demonstrated by the experimental results achieved for the system in section 3. In this sense, we are able to extend the OPD range far beyond compared to previous schemes. On one hand, CSE is avoided by strategically allocating the interferometric structure. On the other hand, a balanced photodetection (BPD) is employed to permit the measurement of low OPDs values in comparison with [17, 18] by eliminating the influence of the baseband component. In addition, sensitivities around 60 dB are achieved after the BPD operation with penetration depth values up to 1 cm. Finally, the main ideas and results are summarized in conclusion section.

II. THEORETICAL DESCRIPTION OF THE MWP-LCI STRUCTURE FOR MULTILAYERED SAMPLES

In the literature, several adaptations of LCI techniques are proposed in order to exploit its benefits from many perspectives and focusing on different capabilities. From our point of view, the application of MWP technology to these techniques enables the possibility to achieve numerous advantages due to the benefits that the operation in the electrical and optical domains can simultaneously offer. In order to present our work, a theoretical analysis is present in this section through the proposed scheme in Fig. 1.

Firstly, an incoherent optical source is considered as input optical signal which is generally described by the optical power spectral distribution $S(\omega)$. Following, an amplitude modulation is performed by means of an intensity electro-optic modulator (MOD). This process is described by $m(t)=1+m_{EOM}\cdot\cos(\Omega)$ in the time domain, where m_{EOM} represents the modulation index and Ω represents the frequency of the RF tone introduced in the modulation

process. After the modulator, the optical signal is launched into a dispersive element characterized by the optical transfer function $H_{DE}(\omega)$, which can be defined as:

$$\tilde{H}_{DE}(\omega)=e^{-\frac{\alpha}{2}L}\cdot e^{-j\varphi(\omega)}\ \text{ with}$$

$$\varphi(\omega)=\varphi_0+\varphi_1(\omega-\omega_0)+\frac{1}{2}\varphi_2(\omega-\omega_0)^2 \qquad (1)$$

where α represents the attenuation, L is the length of the dispersive element, φ_0 is the propagation constant for the optical frequency ω_0, φ_1 a parameter related to the delay and φ_2 the dispersion characteristic of the element also for the optical frequency ω_0.

Once the optical signal is propagated through the dispersive element, a conventional LCI interferometric structure is located in the scheme [12] and defined with the optical transfer function $H_{INTERF}(\omega)$. In one of the arms, the sample under test is placed, characterized by its optical transfer function $H(\omega)$. In the other arm, the reference mirror is located and described by $R_M(\omega)$ [2]. Our MWP-LCI system uses both output optical ports of the interferometric structure. The corresponding transfer functions for both output ports of the interferometer are given by:

$$\tilde{H}_{INTERF}^{out1}(\omega)=\frac{j}{2}\Big(\tilde{H}(\omega)\cdot e^{-2j\omega\tau_S}-\tilde{R}_M(\omega)\cdot e^{-2j\omega\tau_R}\Big)$$

$$(2)$$

$$\tilde{H}_{INTERF}^{out2}(\omega)=\frac{1}{2}\Big(\tilde{H}(\omega)\cdot e^{-2j\omega\tau_S}+\tilde{R}_M(\omega)\cdot e^{-2j\omega\tau_R}\Big)$$

where τ_R is the delay related to the optical path between the fiber coupler and the reference mirror surface and τ_S is the delay associated to the optical path from the fiber coupler to the end of the fiber in the sample arm. The factor 2 in the exponentials refers to the round-trip path length to the reflective surface.

Here, some considerations are made for defining the sample and the reference mirror. In this case, the sample under test will be composed of 'n' layers [2], each of them separated a distance given by the delay τ_n and with a reflectivity index H_n. For the reference mirror, a constant and complex reflectivity factor will be considered. This is mathematically expressed as:

$$\tilde{H}(\omega)=\sum_n H_n\cdot e^{-2j\omega\tau_n}\ ;\ \tilde{R}_M(\omega)=R_M \qquad (3)$$

After the reflection of the optical signal in each arm of the interferometer, the resultant contributions are driven again to the fiber coupler where both are combined, producing the interference pattern. Finally, the photodetection is performed to obtain the photocurrents $i_1^{out}(t)$ and $i_2^{out}(t)$ through the detector PD1 and PD2, respectively. This process is generally described by:

$$i_{1,2}^{out}(t)=\Re\cdot\left\langle\left|e_{1,2}^{out}(t)\right|^2\right\rangle=\Re\frac{1}{2\pi}I_{1,2}^{out}(\Omega)\cdot e^{j\Omega t}+c.c. \qquad (4)$$

where $e_1^{out}(t)$ and $e_2^{out}(t)$ represent the electric field before the photodetection in PD1 and PD2, respectively (see Fig. 1).

Taking into account Eq. (1) and Eq. (2), an analysis similar

to [16] is followed from Eq. (4) in order to obtain the amplitude responses $I_1^{out}(\Omega)$ and $I_2^{out}(\Omega)$ for the harmonic RF contribution Ω, which is detected in PD1 and PD2, respectively:

$$I_{1,2}^{out}(\Omega) = \left[\frac{m_{EOM}}{2} e^{-\alpha L} e^{-j\Omega(\varphi_1 + 2\tau_0)} \right] \cdot$$

$$\left[\underbrace{\sum_n \left(\cos\left(\frac{1}{2}\varphi_2\Omega^2 \right) \cdot \tilde{I}(\Omega) \cdot \left[\left(|H_n|^2 e^{-j2\Omega\tau_n} e^{j\Omega\Delta\tau} \right) + \left(|R_M|^2 e^{-j\Omega\Delta\tau} \right) \right] \right)}_{DC(\Omega=0)} \right.$$

$$+ \underbrace{\sum_n \sum_{m\neq n} e^{-j\Omega(\tau_n + \tau_m)} \cos\left(\frac{1}{2}\varphi_2\Omega(\Omega - \Omega_{nm}') \right) H_n \cdot H_m^* \cdot \tilde{I}(\Omega - \Omega_{nm}')}_{BB(\Omega=\Omega_{nm})}$$

$$\pm \underbrace{\sum_n \left(e^{-j\Omega\tau_n} \cdot \cos\left(\frac{1}{2}\varphi_2\Omega(\Omega - \Omega_n') \right) \cdot H_n \cdot R_M^* \cdot \tilde{I}(\Omega - \Omega_n') \right)}_{LCI(\Omega=+\Omega_n')}$$

$$\left. \pm \underbrace{\sum_n \left(e^{-j\Omega\tau_n} \cdot \cos\left(\frac{1}{2}\varphi_2\Omega(\Omega + \Omega_n') \right) \cdot H_n^* \cdot R_M \cdot \tilde{I}(\Omega + \Omega_n') \right)}_{LCI(\Omega=-\Omega_n')} \right]$$

$$(5)$$

where τ_0 and $\Delta\tau$ represent reference delays for the interferometer arms (τ_R and τ_S), defined as:

$$\tau_0 = \frac{\tau_S + \tau_R}{2} \quad ; \quad \Delta\tau = \tau_R - \tau_S \qquad (6)$$

and $I(\Omega)$ represents the Fourier Transform (FT) of the optical source scaled to the electrical frequency, given by:

$$\tilde{I}(\Omega) = \frac{1}{2\pi} \int_{-\infty}^{\infty} I(\omega) \cdot e^{-j\omega\varphi_2\Omega} d\omega \qquad (7)$$

From Eq. (5), we can distinguish different terms. First, a DC contribution is found which depends on the power spectral density of the source and the square modulus of each sample contribution $|H_n|^2$ and the optical transfer function of the reference mirror. This DC co is located around baseband, i.e., $\Omega=0$. Secondly, a baseband (BB) component appears in Eq. (5) which is located at low values of Ω. This term is related to the crosstalk between different layers. Nevertheless, as the difference in delay between these layers is very low compared to the delays produced by each individual layer, these crosstalk reflection terms are frequencially far from the following contributions, which represents the MWP-LCI response. Different slight contributions are located at the RF frequency $\Omega_{nm}' = (\tau_n - \tau_m)/\varphi_2$.

The third term of Eq. (5) represents the RF resonance produced after the photodetection process and its central frequency is dependent on the Optical Path Difference (OPD) between the arms of the interferometer. The central frequency of the resonance measured in the system (Ω_n') is closely related to the delay associated to the 'nth' layer of the sample (τ_n). In this case, both magnitudes are related by the dispersive element and by the delay between the arms of the interferometer $(\Delta\tau)$:

$$\tau_n' = -\varphi_2\Omega_n' \quad \text{with} \quad \tau_n' = 2(\tau_n - \Delta\tau) \qquad (8)$$

Note that in order to obtain positive delay values (τ_n'), the central frequency of the resonance measured (Ω_n') must also have a positive frequency value. This fact sets up two conditions to the system: the parameter ϕ_2 must have a negative value and the difference in delays between both arms $(\Delta\tau)$ must have a lower value than the delay produced by the considered layer of the sample (τ_n). This component is the desired contribution for LCI techniques since, after its analysis, key parameters as sensitivity or resolution can be calculated. Finally, a last term with the same amplitude as the third contribution of Eq. (5) is observed. However, the produced resonance, in this case, is located in the negative part of the frequency axis. The sign $\pm$ in Eq. (5) differentiates each contribution at the outputs of the interferometer. Concretely, the output 1 corresponds to (-) and output 2 to (+) where the DC and BB terms are common for both expressions.

From Eq. (8), a linear relationship is demonstrated between the optical delay OPD_n associated to the 'nth' layer of the sample and the central frequency for the measured RF resonance Ω_n. This relationship is based on the dispersive element which is characterized by φ_2. Taking into account Eq. (8), we can define the OPD as:

$$OPD_n = c_0 \cdot \tau_n = c_0 \left[-\frac{\varphi_2\Omega_n'}{2} + \Delta\tau \right] \qquad (9)$$

with c_0 representing the speed of light in vacuum.

From the structure of Fig. 1, we can observe that a balanced photodetection (BPD) is performed to finally obtain the desired contribution, i.e., $i_{out}(t) = i_2^{out}(t) - i_1^{out}(t)$. Taking into account both expressions of the interferometer seen in Eq. (2), the final equation for the amplitude term, $I_{out}(\Omega)$, is given by:

$$I_{out}(\Omega) \approx \left[e^{-j\Omega(\varphi_1 + 2\tau_0)} \right] \cdot$$

$$\left[\sum_n \left(e^{-j\Omega\tau_n} \cdot m \cdot \cos\left(\frac{1}{2}\varphi_2\Omega(\Omega - \Omega_n') \right) \cdot H_n \cdot R_M^* \cdot \tilde{I}(\Omega - \Omega_n') \right) \right]$$

$$(10)$$

With Eq. (10) we have demonstrated that, due to the performance of a balanced photodetection in the system, the DC term and BB component are eliminated, making possible to distinguish the RF resonances that are generated at low frequencies and consequently, at low OPD values. In this case, the term that appears in the negative part of the frequency axis (as described in Eq. (5)), should be present in Eq. (10). However, we do only consider positive values for the central frequency of the produced resonance.

As previously mentioned, an amplitude modulation is generated by an intensity electro-optic modulator. In principle, Carrier Suppression Effect (CSE) would be present in the system when this modulation format is employed along with a link fiber as dispersive element [17]. However, the CSE term is slightly different from its typical version [18]. From (10), we observe that CSE effect is shifted to the own RF frequency Ω_n corresponding to the measured OPD_n, being negligible around the frequencies where the RF resonances are produced. This fact permits to employ a full RF frequency range as CSE
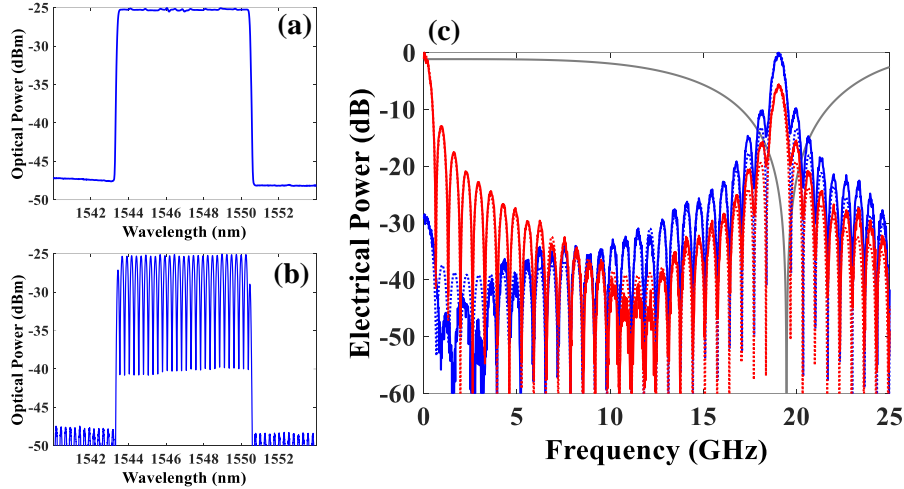
Fig. 2. (a) Optical spectrum when a uniform profile of 8.8 nm bandwidth is considered as the optical source. (b) Optical spectrum at the output of the interferometer when an OPD of 8.2 mm is set. (c) Electrical transfer function of the MWP-LCI structure when single detection (─) and balanced detection (─) are performed. Computer simulations are added in dashed line for each detection format, along with the CSE for a -220 ps² dispersive element (─).

is avoided even using a simple amplitude modulation.

III. EXPERIMENTAL RESULTS

A. *Principle of operation*

In this section, the principle of operation is described through the experimental setup, which is implemented according to the MWP-LCI structure of Fig. 1. The optical signal is generated by the combination of a Broadband Source (BBS) with an optical bandwidth close to 80 nm (ASE-CL-20-S-NP Photonics) and an Optical Channel Controller (OCC) (Peleton QTM100C). The OCC is centered at 1546.92 nm and has 48 channels with a 3dB bandwidth of 0.8 nm. The attenuation of each OCC channel can be independently controlled. Then, an amplitude modulation is performed in a 40 GHz modulator by means of a Vector Network Analyzer (VNA) (Agilent E8364A) which provides an RF tone as electrical input. Following, a single mode fiber (SMF) is considered as dispersive element, characterized by a chromatic dispersion parameter of φ_2=-220 ps².

In the experimental setup, a Mach-Zehnder Interferometer (MZI) is considered as interferometric structure by employing two concatenated 2x2 optical couplers. In one of the arms, a polarization controller device has been placed along with a Variable Optical Attenuator (VOA) in order to ensure the maximum visibility of the interference pattern generated. In the other arm, the sample is placed. The interferometer is the key element that generates the slicing of the optical signal, which is directly related to the OPD. Experimentally, in order to simulate the behavior of a layer from a real sample, a Variable Delay Line (VDL) is placed in the sample arm. This device can be manually set to generate a controlled OPD. The result of the slicing process can be observed in Fig. 2(b) for a sample with an OPD value of 8.2 mm. Finally, both arms of the interferometer are connected to the inputs of a balanced photodetector (BPD) which has a total bandwidth of 50 GHz. Finally, the performance of the MWP-LCI structure with balanced detection is analyzed by means of the electrical transfer function of the system measured in the range from 0-25 GHz using a VNA.

Firstly, in order to show the performance of the proposed MWP-LCI structure with balanced detection, a one-layer sample with an OPD of 8.2 mm is considered. The power spectral density of the optical source is configured as a uniform profile with 8.8 nm bandwidth (see Fig. 2(a)). Moreover, a -220 ps² accumulated dispersion parameter (φ_2) is considered. The results obtained are shown in Fig. 2(c). We can observe that a RF resonance around 19 GHz is generated, according to Eq. (10), when balanced detection is considered. The central frequency of this component is directly related to the OPD of the sample located in the interferometric structure, as described in Eq. (9). In order to compare properly the obtained results with previous proposals [16-18], Fig. 2(c) includes the RF response when single detection approach is measured. As shown in Eq. (5), a DC component is present, compromising the sensitivity measurements of low OPD values. This implies a really relevant fact as the presence of a DC contribution in the single detection LCI based systems [16-18] involves a limitation in the OPD range resulting in a sensitivity decrease for low OPD values. For our balanced scheme, it can be seen that the baseband component is considerably reduced (around 30 dB). Furthermore, if the amplitude of the RF resonance is compared for both detection approaches, we observe that a 6 dB improvement is achieved what also implies an improvement in the sensitivity in the whole OPD range.

On the other hand, we can also observe that the RF resonance is not affected by CSE with the strategic allocation of the interferometer. Note that CSE response is plotted in Fig. 2(c) with a notch filter close to the central frequency of the sample. This enables the possibility to reach higher penetration depths compared to [16]. Theoretical simulations from Eq. (5) and (10) are included in Fig. 2(c) in order to validate the data obtained experimentally where an excellent agreement is achieved.

B. *System performance for multilayered operation*

In order to experimentally demonstrate the system performance under multilayered operation, a two-layered
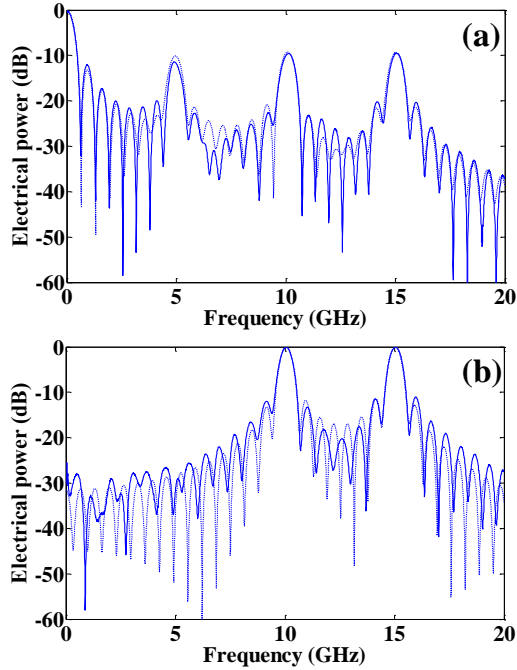
Fig. 3. Electrical transfer function of the MWP-LCI structure when (a) single and (b) balanced photodetection when a two-layered sample is considered. OPDs of the sample are set to 4.33 mm and 6.50 mm. Theoretical simulation of Eq. (10) has been added in dashed line.

sample is taken into account to show the potential of the proposed MWP-LCI structure to characterize a general multilayer sample. In this way, two VDLs are considered in the sample and set to τ_1=4.33 mm and τ_2=6.50 mm. Experimental and theoretical results are shown in Fig. 3. On the one hand, Fig. 3(a) shows the electrical transfer function for the single optical output coming from the detector PD1. On the other hand, Fig. 3(b) represents the electrical response for balanced photodetection. Firstly, two RF resonances are generated around f_1 =10 and f_2 =15 GHz as a result of the two-layered sample created by the VDLs as predicted in Eq. (9). Comparing single and balanced photodetection in Fig. (3), we observe that Fig. 3(a) shows the DC contribution located around Ω=0 and the crosstalk contribution due to the interference between both layers τ_1 and τ_2. Indeed, a residual RF resonance appears around the RF frequency $f_{21} = f_2 - f_1 = 5$ GHz as previously mentioned. Both DC and BB contributions are successfully minimized in Fig. 3(b), overcoming the limitation of the previous MWP-LCI schemes [16]. Additionally, computer simulation of the electrical transfer function has been added to Fig. 3 when two layers are considered to prove the excellent agreement achieved between theoretical and experimental results.

As abovementioned, initial MWP-LCI approaches are only demonstrated for one-layered samples. In these cases, just the DC term is present and the BB term is not critical because self-reflection contribution only appears in a multilayered scenario. As a consequence of the one-layer analysis, not all degrading factors are shown what does not leave extent the presence of these limiting factors. Equation (10) of the multilayered theory development shows the elimination of both DC and BB contributions by the intrinsic characteristics
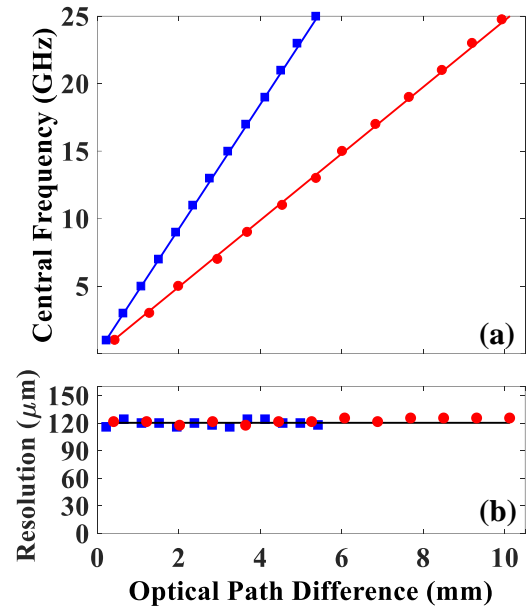

Fig. 4. Central frequency of the RF resonance generated when different OPD values are set in the interferometer for -220 ps^2 (■) and -440 ps^2 (●) dispersive elements Theoretical results of Eq. (9) have been added in solid line. (b) Resolution of the MWP-LCI structure for different OPDs when a -220 ps^2 (■) and -440 ps^2 (●) dispersive elements are considered. Theoretical value of the resolution has been added in solid line.

of our proposed MWP-LCI structure, independently of the kind of employed sample. The elimination of both terms (DC and BB) permits to increase the sensitivity and the operation range of the system, and consequently, the penetration depth.

Following, typical LCI parameters as sensitivity, penetration depth and resolution are shown by means of experimental results when balanced detection is employed in the proposed MWP-LCI structure. Firstly, the central frequency of the generated RF resonances is measured when different OPDs are set in the multilayered sample in order to obtain the maximum penetration depth of the system and the testing of the relationship between the OPD under test and the measured RF central frequency. In this way, we consider a -220 ps^2 and a -440 ps^2 accumulated dispersion parameters. Results have been plotted in Fig. 4(a). We can observe that a linear relationship exists between the OPD set in the interferometer and the central frequency of the each RF resonance, showing an excellent agreement with Eq. (9). For this case, slopes of 4.67 and 2.52 MHz/μm have been measured for the -220 ps^2 (■) and -440 ps^2 (●) cases, respectively. As pointed out previously, the balanced detection is able to remove the DC and BB components. Due to this fact, the OPD range can be extended to values close to 0 mm, since the RF resonances produced in this range are not affected by them. For the dispersive elements considered, maximum penetration depths of 5.5 mm and 10 mm are achieved for -220 ps^2 and -440 ps^2, respectively. By observing Fig. 4(a) and Eq. (9), we can also conclude that higher penetration depths can be obtained by employing larger accumulated dispersions.

Furthermore, the resolution achieved by the structure has been experimentally evaluated. In conventional LCI techniques, the axial resolution (δz) is proportional to $\lambda^2/\Delta\lambda$ where $\Delta\lambda$ is the optical source bandwidth and λ corresponds to the central operation wavelength of the optical source.
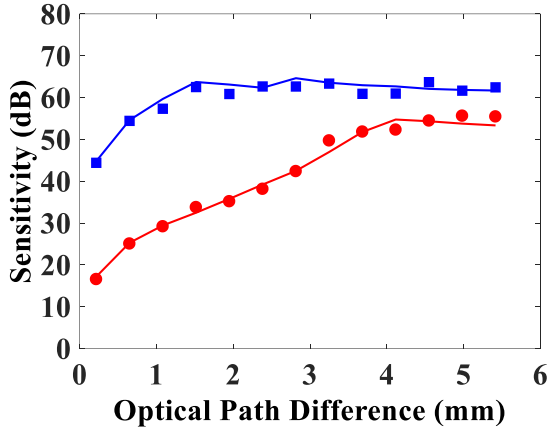
Fig. 5. Sensitivity of the system versus the central frequency of the RF resonance when single detection (●) and balanced detection (■) are performed. Theoretical simulations of the sensitivity achieved by the system has been added in solid line.

Attending to MWP-LCI systems, resolution is obtained from the bandwidth of a RF resonance, i.e., its 3dB bandwidth (BW_{elec}). At the same time, this 3 dB bandwidth is related to the optical bandwidth of the source as in classical LCI [2]. In this way, resolution for MWP-LCI can be obtained as:

$$\delta z = c_0 \pi \varphi_2 BW_{elec} \qquad (11)$$

Therefore, the electrical bandwidth of the RF resonance for different OPD values is measured in order to obtain resolution. For this, the same optical power source profile as seen in Fig. 2(a) and -220 ps^2 (■) and -440 ps^2 (●) dispersive elements are considered. Fig. 4(b) shows the experimental and theoretical results. The theoretical simulation of the resolution obtained by Eq. (11) has also been added to the graph in solid line. A quasi-invariant resolution through all the OPD range measured is obtained for both scenarios. A resolution value around 120 μm is experimentally obtained for both dispersive elements, showing an excellent agreement with the theoretical result. Note that the same resolution is obtained for both dispersive elements. This fact is caused by the scaling factor produced by φ_2. The increment of the dispersion value results in a decrement of the 3dB bandwidth and vice versa. In this sense, when we apply Eq. (11) we observe that the use of a more or less dispersive element does not result in an increment or decrement of the resolution. However, the change in the dispersive element does imply other factors, as the additional optical losses, what affects the sensitivity of the overall MWP-LCI system.

Finally, the sensitivity of the MWP-LCI system is obtained. In conventional LCI, sensitivity is a parameter that describes the minimum reflectivity that can be measured. Experimentally, this can be done by measuring the electrical transfer function of the structure when the sample is present in the structure ($H_n=1$) and when it is not ($H_n=0$). Then, for each OPD, the amplitude difference of both electric transfer functions will represent the sensitivity of the system. If we consider $H_n=0$ in Eq. (5), it can be observed that no RF resonance is generated, and the remaining term is completely produced by the baseband contribution. Consequently, by using the balanced detection approach it is possible to obtain

an important sensitivity improvement since the baseband term is considerably reduced.

In order to demonstrate the sensitivity improvement compared to previous proposals [16-18], we obtain the electrical transfer function for single and balanced detection approaches. The same optical power profile as seen in Fig. 2(a) and a -220 ps^2 dispersive element have been considered in this case. Results are depicted in Fig. 5. It can be observed that in the range of 0-3.5 mm the sensitivity achieved by the balanced detection scheme (■) is much higher compared to the single detection. Differences of 30 dB can be observed between both detection approaches. This fact is mainly produced by the high reduction of the baseband component achieved by the structure. In the range of 3.5-5.5 mm, we observe a difference near to 6 dB between both approaches caused by the improvement in the RF resonance amplitude when the balanced detection is employed. Moreover, we can also observe from Fig. 5 that a maximum sensitivity value of 55 dB is achieved for single detection but in a very limited range of OPDs (4.5-5.5 mm). However, an average sensitivity of 62 dB is obtained for the balanced detection approach additionally with a very wide OPD range (1.5-5.5 mm). In Fig. 5, we show in solid lines the excellent agreement between theoretical and experimental results in sensitivity for both approaches.

IV. CONCLUSION

In this paper, we have presented an advanced structure for the application of Microwave Photonics (MWP) technology to Low Coherence Interferometry (LCI) in order to retrieve the visibility of low-coherence interferograms. A theoretical analysis of the scheme has been addressed in order to provide the basis for the correct comprehension of the relation between LCI and MWP when considering a discrete layered model for the sample. Compared to previous contributions, the novel allocation of the interferometric structure and the introduction of balanced detection permit to improve the performance of the previous MWP-LCI system for any interrogated multilayered sample. Note that previous schemes are limited to a one-layered sample. We have also experimentally demonstrated the retrieval of the interference pattern for one-layer and two-layer sample scenario through a dispersive element, obtaining an excellent agreement with the theoretical results detailed in this work. In this sense, the experimental demonstration of one-layered and two-layered sample proves the scalability of the MWP-LCI concept, which is theoretically generalized for a multilayered scenario. Moreover, several limitations are overcome with the MWP-LCI proposal compared to previous proposals [16-18]. Due to the strategic allocation of the interferometer, penetration depth achieved is increased since the CSE is intrinsically avoided by the structure. In this case, a maximum depth of 1 cm has been achieved with an almost invariant resolution value of 120 μm through the whole measured range. Nevertheless, it is important to note that the penetration depth in MWP-LCI is also limited by the resolution and sensitivity values. On the one hand, in a system composed of electrical and electro-optical devices, there is an unavoidable dependency of these

devices with frequency, what can limit the maximum penetration depth if the sensitivity loss is too high. On the other hand, the use of a non-ideal dispersive element in an experimental setup, also causes a resolution loss for high values of the OPD. This fact is mainly due to the dispersion characteristics of the dispersive element. Concretely, the third-order dispersion. These limitations will be studied in future works. Finally, in the case of the sensitivity, an important improvement has been experimentally demonstrated. Due to the balanced detection, the baseband component can be highly reduced, contributing to an improvement of the sensitivity for low OPD values. An average sensitivity of 62 dB has been experimentally demonstrated in a wide OPD range.

REFERENCES

[1] Y. J. Rao and D. A. Jackson, "Recent progress in fiber optic low-coherence interferometry," *Meas. Sci. Technol.*, vol. 7, no. 7, pp. 981–999, 1996.

[2] M. Wojtkowski, "High-speed optical coherence tomography: basics and applications," *Appl. Opt.*, vol. 49, no. 16, pp. 30-61, 2010.

[3] R. Gabet, E. Le Cren, C. Jin, M. Gadonna, B. Ung, P. Sillard, H. G. Nguyen, Y. Jaouën, M. Thual and S. LaRochelle, "Complete Dispersion Characterization of Few Mode Fibers by OLCI Technique," *J. Lightwave Technol.*, vol. 33, no. 6, pp. 1155-1160, 2015.

[4] H. Liang, B. Peric, M. Hughes, A. Podoleanu, M. Spring and D. Saunders, "Optical coherence tomography for art conservation and archaeology," *Proc. SPIE*, vol. 6618, 2007.

[5] Y. Wang, J. Gong, B. Dong, W. Bi, and A. Wang, "A quasi-distributed sensing network with time-divisionmultiplexed fiber Bragg gratings," *IEEE Photon. Technol. Lett.*, vol. 23, no. 2, pp. 70–72, 2011.

[6] J. Fujimoto and D. Huang, "Foreword: 25 Years of Optical Coherence Tomography," *Invest. Ophthalmol. Vis. Sci.,* vol. 57, no. 9, pp. OCTi-OCTii, 2016.

[7] M. J. Suter, G. J. Tearney, W. Y. Oh and B. E. Bouma, "Progress in Intracoronary Optical Coherence Tomography," *IEEE J. Sel. Top. Quantum Electron.*, vol. 16, no. 4, pp. 706-714, 2010.

[8] C. K. Lee, T.T. Chi, C. T. Wu, M. T. Tsai, C. P. Chiang and C. C. Yang, "Diagnosis of oral precancer with optical coherence tomography," *Biomed. Opt. Express*, vol. 3, no. 7, pp. 1632-1646, 2012.

[9] Z. G. Wang, C. Lee, W. Waltzer, Z.J. Yuan, Z.L. Wu, H.K. Xie and Y.T. Pan, "Optical Coherence Tomography for Noninvasive Diagnosis of Epithelial Cancers," *Conf. Proc IEEE Eng Med Biol Soc*, WeC09.4, pp. 129-132, 2006.

[10] M. R. Lee and J. A. Izatt, E. A. Swanson, D. Huang, J. S. Schumun, C. P. Lin, C. A. Puliafito and J. G. Fujimoto, "Optical coherence tomography for ophthalmic imaging: new technique delivers micron-scale resolution," *IEEE J. Sel. Top. Quantum Electron.*, vol. 14, no. 1, pp. 67-76, 1995.

[11] B. M. Kim, H. W. Jeong, J. Kim, S. W. Lee and W. Chung, "Full range, dual depth optical coherence tomography for ophthalmology," in *2013 Conference on Lasers and Electro-Optics Pacific Rim (CLEOPR)*, Kyoto, pp. 1-2, 2013.

[12] A. Gh. Podoleanu, "Optical Coherence Tomography," *J. Microsc.*, vol. 247, no. 3, pp. 209-219, 2012.

[13] J. Capmany and D. Novak, "Microwave photonics combines two worlds," *Nat. Photon.*, vol. 1, no. 6, pp. 319–330, 2007.

[14] A. L. Ricchiuti, D. Barrera, S. Sales, L. Thevenaz, and J. Capmany , "Long fiber Bragg grating sensor interrogation using discrete-time microwave photonic filtering techniques," *Opt. Express*, vol. 21, no. 23, pp. 28175-28181, 2013.

[15] L. Hua, Y. Song, J. Huang, X. Lan, Y. Li, and H. Xiao, "Microwave interrogated large core fused silica fiber Michelson interferometer for strain sensing," *Appl. Opt.*, vol. 54, no. 24, pp. 7181-7187, 2015.

[16] C. R. Fernandez-Pousa, J. Mora, H. Maestre, P. Corral "Radio-frequency low-coherence interferometry," *Opt. Lett.*, vol. 39, no. 12, pp. 3634-3637, 2014.

[17] J. Mora, M. Bolea and J. Capmany, "Novel approach for Low Coherence Interferometry based on a microwave photonic architecture," in *2015 17th International Conference on Transparent Optical Networks (ICTON)*, pp. 1-4, 2015,

[18] J. Benítez, M. Bolea, J. Mora, "High-performance low coherence interferometry using SSB modulation", *IEEE Photon. Technol. Lett.* vol. 29, no. 1, pp. 90-93, 2017.